Journal of Power Sources 196 (2011) 4382–4387

Contents lists available at ScienceDirect

Journal of Power Sources

journal homepage: www.elsevier.com/locate/jpowsour

CuO/CeO_2 supported on Zr doped SBA-15 as catalysts for preferential CO oxidation (CO-PROX)

Álvaro Reyes-Carmona[a], Ana Arango-Díaz[a], Elisa Moretti[b], Aldo Talon[b], Loretta Storaro[b], Maurizio Lenarda[b], Antonio Jiménez-López[a], Enrique Rodríguez-Castellón[a,*]

[a] Departamento de Química Inorgánica, Cristalografía y Mineralogía (Unidad Asociada al ICP-CSIC), Facultad de Ciencias, Universidad de Málaga, Campus de Teatinos, 29071 Málaga, Spain
[b] INSTM and Dipartimento di Chimica, Università Ca' Foscari di Venezia, Via Torino 155/b 30172 Mestre-Venezia, Italy

ARTICLE INFO

Article history:
Received 6 August 2010
Received in revised form
24 September 2010
Accepted 5 October 2010
Available online 13 October 2010

Keywords:
Hydrogen purification
Fuel cell
CO-PROX
CuO/CeO_2

ABSTRACT

The application of the catalytic system CuO/CeO_2 supported on Zr doped SBA-15 mesoporous silica to the preferential oxidation of CO on hydrogen streams (CO-PROX) suitable to be used to feed PEM fuel cells, has been studied. A loading of 20% (wt.) Ce and 6% (wt.) Cu was found optimal for the CO-PROX reaction. The influence of the presence of CO_2 and H_2O in the gas feed was also studied in order to simulate the real operation conditions of a PEMFC feed stream generated by alcohol steam reforming. The catalysts were characterized by XRD, adsorption–desorption of N_2 at −196 °C, TEM, $-H_2$-TPR and XPS. The system reducibility was found modified by the incorporation of zirconium in the support, with improvement of both the conversion and selectivity of the catalytic system, compared to the same material without Zr.

1. Introduction

Hydrogen suitable to feed proton exchange membrane fuel cells (PEMFCs) can be produced by reforming of alcohols or hydrocarbons, in case followed by water–gas shift reaction. The reformed gas obtained still contains variable amounts of CO, which will decrease the energy efficiency of the fuel cell because CO-induced poisoning of the Pt anode catalyst. There are several methods to eliminate CO from the hydrogen rich gas stream, such as selective CO methanation, selective diffusion through membranes, but preferential oxidation of CO (CO-PROX) is the most economical and efficient approach both for static and mobile applications to reduce CO to the desired level without excessive hydrogen consumption [1–7].

Several catalytic systems based on supported very expensive noble metals (Au, Pt, Ru) have been proposed but CuO/CeO_2 based oxide systems seem to be a selective, thermally stable and low cost alternative catalyst [8–11]. The particular ability of these CO-PROX catalysts was essentially attributed to the synergistic redox properties of copper–ceria interfacial sites [12–18]. This system has been studied by different authors finding that the preparation methods and the Cu loading are determinant for the performance of the CuO/CeO_2 catalysts [13,21]. The presence of Zr was found to modify the redox properties of the Cu/Ce pair, improving the catalytic results [11]. The presence of CO_2 and H_2O in the feed stream decreases the formation of Cu^+-carbonyls, indicative of CO oxidation [19]. Recently it was observed that the segregation of Cu and the formation of metallic Cu are involved in the partial deactivation of CO-PROX catalysts [20].

In this work a CuO/CeO_2 system supported on different mesoporous silica doped with zirconium is studied. The materials were characterized before and after the CO-PROX reaction, by XRD, adsorption–desorption of N_2 at −196 °C, TEM, H_2-TPR and XPS in order to find possible correlations between composition, structure and catalytic performance.

2. Experimental

2.1. Catalyst preparation

The mesoporous Zr doped SBA-15 silica (SBAZr10) was prepared according to the method proposed by Szczodrowski et al. [22] with Si/Zr atomic ratio = 10. Besides, a SBA-15 sample (SBA) was prepared following the synthetic method described by Gómez-Cazalilla et al. [23]. An additional support material ($SBAZrO_2$) was prepared by incipient wetness impregnation of a pure silica SBA-15 using a zirconium(IV) acetate solution, with an atomic ratio Si/Zr = 10, and then calcined for 6 h at 550 °C with a heating ramp of 1 °C min^{-1}. The active phase was incorporated

* Corresponding author. Tel.: +34 952131873; fax: +34 952137534.
E-mail address: castellon@uma.es (E. Rodríguez-Castellón).

0378-7753/$ – see front matter © 2010 Elsevier B.V. All rights reserved.
doi:10.1016/j.jpowsour.2010.10.019

by incipient wetness impregnation using an aqueous solution of copper(II) and cerium(III) acetates. The loading of copper was 6 wt.% and cerium was 20 wt.%. Due to the limited solubility of the salts used, the impregnation was made in several steps until the total incorporation of the salts. All samples were dried 12 h at 60 °C and then calcined at 550 °C for 4 h with a heating ramp of 1 °C min^{-1}. The catalysts were labeled *Y*Ce20Cu6, where *Y* denoted the used support (SBAZr10Ce20Cu6, SBACe20Cu6, SBAZrO$_2$10Ce20Cu6 respectively).

2.2. Catalytic tests

Catalytic activity tests were carried out in a laboratory flow apparatus, with a fixed bed reactor operating at atmospheric pressure. The catalysts (0.100 g), with a defined particle size (0.050–0.110 mm) were introduced into a tubular Pyrex glass reactor (5 mm i.d.), and placed inside an aluminum heating block.

Before the catalytic experiments, the samples were heated in situ at 400 °C under flowing air for 1 h. The contact time *W*/*F* was 0.18 g s cm^{-3} (GHSV = 22 000 h^{-1}). The reaction mixture composition was 1.25% CO, 1.25% O_2, 50% H_2, balanced with He. The effect of CO_2 and H_2O was examined in separate runs with the addition of 15 vol.% CO_2 and 10 vol.% H_2O. An ice-cooled cold finger was used to trap the excess of water downstream from the reactor. A HP6890 CG gas chromatograph equipped with a thermal conductivity detector (TCD) was used to analyze the outlet composition. A CP Carboplot P7 column was used, with helium as carrier. The detector limit for CO was 10 ppm. The temperature was varied in the 40–190 °C range, and measurements were carried out till a steady state was achieved.

The carbon monoxide (Eq. (1)) and oxygen (Eq. (2)) conversions were calculated based on the CO and O_2 consumption, respectively:

$$X_{CO}(\%) = \frac{n_{CO}^{in} - n_{CO}^{out}}{n_{CO}^{in}} \times 100 \quad (1)$$

$$x_{O_2}(\%) = \frac{n_{O_2}^{in} - n_{O_2}^{out}}{n_{O_2}^{in}} \times 100 \quad (2)$$

The selectivity towards CO_2 was calculated by (Eq. (3)):

$$Sel_{CO_2}(\%) = \frac{n_{CO}^{in} - n_{CO}^{out}}{2(n_{O_2}^{in} - n_{O_2}^{out})} \times 100 \quad (3)$$

and the excess of oxygen factor (λ) is defined as (Eq. (4)):

$$\lambda = 2 \times \frac{n_{O_2}^{in}}{n_{CO}^{in}} \quad (4)$$

In all the catalytic tests, $\lambda = 2$ was used, because this value was previously found optimal for preferential oxidation of CO [10–12].

2.3. Characterization methods

X-ray diffraction (XRD) patterns were obtained with a Philips X'pert PRO apparatus using Cu $K_{\alpha 1}$ radiation (λ = 0.1540 nm) with a Ge (1 1 1) monochromator working at 45 kV and 40 mA. All the measures were made with a step size of 0.0167° in 30 min. High resolution patterns were registered in order to apply the Rietveld method [24] to estimate the average crystallite size, using the same step size but with a total acquisition time of 4 h. The X'pert High Score Plus software was applied for data treatment and calculations, with the standard inner algorithms using pseudoVoigt type curves.

N_2 adsorption–desorption measurements were performed at liquid nitrogen temperature (−196 °C) with an ASAP 2020 apparatus from Micromeritics. Before each measurement, samples were out gassed 12 h at 200 °C and 1×10^{-2} Pa. The specific surface (S_{BET}) was calculated using the BET equation, and the specific pore volume (v_p) was calculated at P/P_0 = 0.98. The pore size distribution was calculated following BJH method, taking the data of the desorption branch and assuming a cylindrical pore model.

Transmission electron micrographs were obtained with a Philips CM200 microscope working at 10 kV. The measurements of X-ray dispersive energy were registered using an EDAX CM200ST probe based in a detector SiLi. The samples were dispersed in 2-propanol and dropped over a Ni grid to avoid interferences in the Cu measurements.

Temperature-programmed reduction of H_2 (H_2-TPR) experiments were carried out using ~0.1 g of freshly calcined catalyst placed in U shaped quartz reactor inside of a tubular oven. In order to remove contaminants, the powders were pre-treated with helium (50 cm^3 min^{-1}) to 150 °C for 1 h. After cooling to ambient temperature, TPR experiments were carried out in 10 vol.% H_2/Ar (30 cm^3 min^{-1}) increasing the temperature from room temperature to 600 °C with a heating ramp of 10 °C min^{-1}, by a temperature programmable controller. The water produced in the reduction was eliminated using a isopropanol–liquid N_2 trap. The hydrogen consumption was calibrated versus CuO and registered using a TCD mounted in a GC Shimazdu 14-B.

X-ray photoelectron spectroscopy (XPS) studies were realized by a Physical Electronic PHI 5700 spectrometer using non monochromatic Mg K radiation (300 W, 15 kV, 1253.6 eV) for the analysis of the core level signals of C 1*s*, O 1*s*, Si 2*p*, Cu 2*p*, Zr 3*d* and Ce 3*d* with a hemispherical multichannel detector. The spectra of powdered samples were registered with a constant pass energy values at 29.35 eV, using a 720 μm diameter circular analysis area.

The X-ray photoelectron spectra obtained were analyzed with PHI ACESS ESCA-V6.0F software and processed using Multipak 8.2B package. The binding energy values were referenced to C 1*s* signal (284.8 eV). Shirley type background and Gauss–Lorentz curves were used to determinate the binding energy. Short acquisition times (<10 min) were used in order to avoid photoreduction of copper and cerium species [25].

3. Results and discussion

3.1. Catalytic tests

The gas stream of the three studied samples was initially fixed to 1.25% CO, 1.25% O_2, 50% H_2 balanced with He. As found in previous works [10–12], the carbon balance showed a good correlation between CO_2 formed and CO consumed. Reverse water gas shift (rWGS) and methanation reactions were found negligible in our experimental conditions and only CO and H_2 oxidations are the reactions considered in these catalytic tests.

The evolution of the conversion of CO and selectivity towards CO_2 curves of the studied catalysts are presented in Fig. 1. All samples showed a good catalytic performance, reaching conversions near 100% at 140 °C. The incorporation of Zr into the support, increases the conversion of CO and the selectivity to CO_2 in comparison with the sample without Zr, labeled as SBACe20Cu6. Both SBAZr samples show a CO conversion of 95% with high selectivity towards CO_2. In the case of SBAZr10Ce20C6, the selectivity towards CO_2 appears to remain close to 100% up to 160 °C. The selectivity loss is caused by the occurrence of the oxidation of hydrogen to water, more thermodynamically favorable at high temperatures.

Since CO_2 and H_2O can be present in significant quantities in reformed gases, the influence of these compounds was evaluated on the best performing sample, SBAZr10Ce20Cu6. The influence of the addition of 15% vol. CO_2 to the feed stream is shown in Fig. 2. As expected and as found previously [12], the addition of CO_2 highly decreases the conversion at reaction temperatures <140 °C. Only at this temperature the conversion reaches the value of 95%. A better

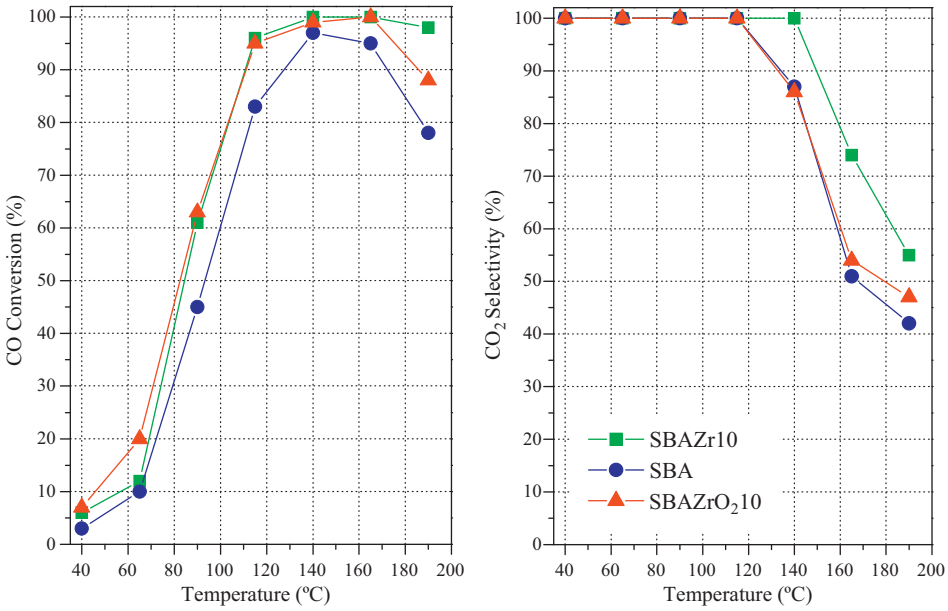

Fig. 1. Conversion and selectivity curves of catalysts YCe20Cu6 on CO-PROX reaction. Operating conditions: 50% H_2, 1.25% CO, 1.25% O_2, He balanced, $\lambda = 2$, GHSV = 22 000 h^{-1}.

approximation to the real operation conditions of a PEMFC feeding system can be studied when both 15% CO_2 and 10% H_2O were added to the feed stream. Both conversion and selectivity fall down drastically, but at 165 °C the sample exhibits a good performance with a conversion of 87% and selectivity towards CO_2 of 72%.

3.2. Characterization

3.2.1. XRD studies

Phase identification was realized on the XRD patterns of both fresh and used samples. The diffractograms of the supports prepared with the Zajác method [22] do not present any peak associated to ZrO_2 phases, while SBAZrO$_2$10 shows the diffractions peaks of the tetragonal ZrO_2 (ISCD #072949) due to the post-synthesis incorporation of that phase at $2\theta = 30.1$, 50.2, 50.6, 59.6 and 60.0°. The diffraction patterns of the studied catalyst are shown in Fig. 3. All fresh catalysts show peaks associated to cubic CeO_2 (cerianite phase, ISCD #072155) at $2\theta = 28.5$, 33.4, 47.5 and 56.5° and monoclinic CuO (tenorite phase, ISCD #043179) at $2\theta = 35.5$ and 38.7° with weak intensities in the samples with SBA and SBAZr10 supports. After the catalytic test, new peaks appeared, associated to metallic Cu, with $2\theta = 43.5$ and 50.4°. If all the intensities of these peaks are compared, the XRD profile of the catalyst based on the SBAZr10 support shows peaks with weaker intensities due to lower reduction degree in comparison to the other studied samples.

Crystallites size of the active phases can be estimated by measuring the contributions to peak broadening using Rietveld methodology to fit the experimental diffractogram with the reference patterns of the detected phases. Average particle sizes for each crystalline phase are summarized in Table 1, showing good values of R_{wp} and particles with nanometric size. The particle size of the crystalline active phases varies with the support. The sizes of cerianite and tenorite are smaller in the case of the pristine SBA-15. With the incorporation of Zr the sizes of the actives phases parti-

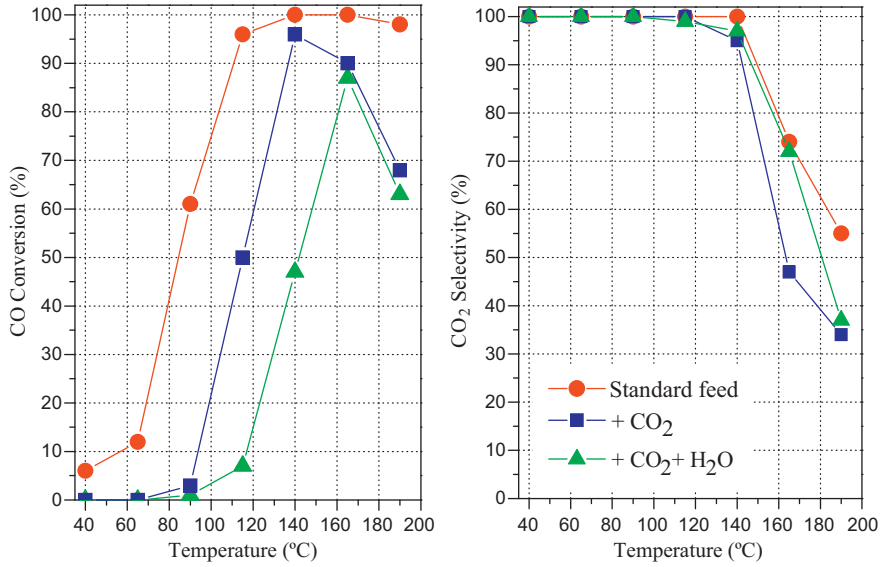

Fig. 2. Influence of CO_2 and H_2O on conversion and selectivity curves of catalysts SBAZr10Ce20Cu6 on PROX reaction. Reaction conditions: 50% H_2, 1.25% CO, 1.25% O_2, 0–15% CO_2, 0–10% H_2O, He balanced, $\lambda = 2$, GHSV = 22 000 h^{-1}.

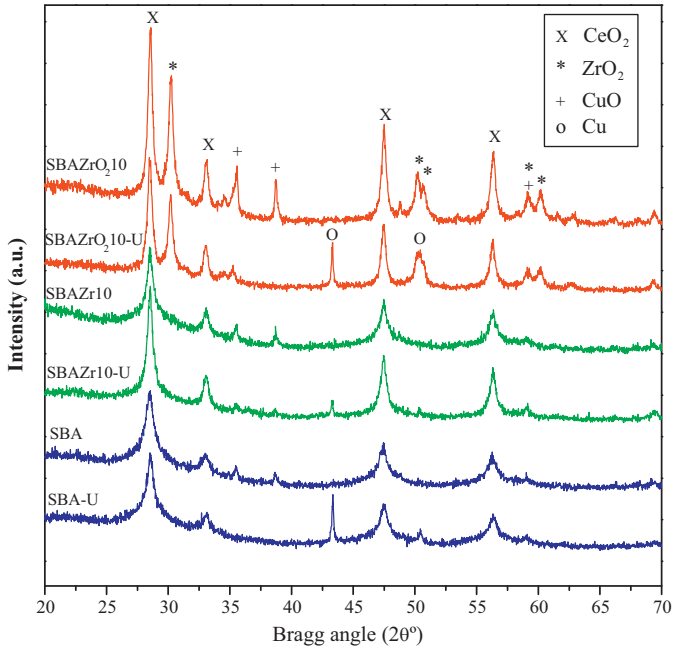

Fig. 3. X-ray diffraction patterns of the samples, fresh and after catalytic test (with –U suffix).

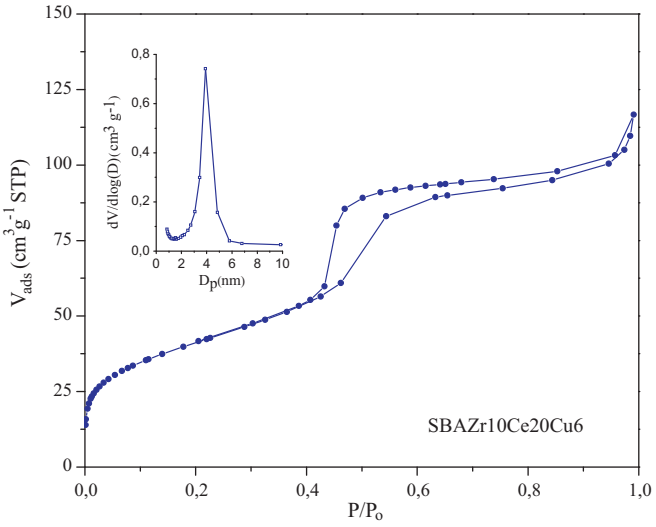

Fig. 4. N_2 adsorption–desorption isotherm at −196 °C and, in the inset, BJH pore size distribution of the sample SBAZr10Ce20Cu6.

Table 2
Textural parameters of the studied catalysts in CO-PROX reaction.

Sample	S_{BET} ($m^2\ g^{-1}$)	V_p ($cm^3\ g^{-1}$)	$D_{p,BJH}$ (nm)
SBAZr10	536	0.53	4.2
SBAZr10Ce20Cu6	147	0.17	3.8
SBA	455	0.47	4.0
SBACe20Cu6	139	0.16	3.8
$SBAZrO_2$10	330	0.35	4.2
$SBAZrO_2$10Ce20Cu6	215	0.27	3.6

cles increase, being bigger in the case of the support $SBAZrO_2$10. In any case nanometric crystallites are obtained, ruling out the formation of solid solutions between phases, in accordance with lattice parameters of cerianite phase, showed in Table 1, and compared with the CeO_2 reference value.

3.3. Surface and textural properties

The specific surface area of the supports and fresh catalysts were studied using the data obtained from adsorption–desorption isotherms of N_2 at −196 °C. All materials show the typical type IV isotherm, according with the IUPAC classification. In Fig. 4, the isotherms of SBAZr10Ce20Cu6 catalyst are graphically presented, showing a H1 hysteresis cycle, according with the behavior of these materials.

The pore size graph, also presented in Fig. 4, shown a narrow distribution centered on the 4–5 nm, corresponding to the mesopores range, typical of SBA-15 based materials. BET area, pore volume and average pore size calculated by the BJH method of all supports and catalysts are summarized in Table 2. All the supports have high specific surface area, typical of these mesoporous materials. The incorporation of the active phase into the supports decreased the specific surface area, while the average pore size remained similar to that of the supports.

The surface data and the information obtained by XRD can be corroborated using TEM. The micrography presented in Fig. 5 shows the morphology of these materials. Clear areas are visible, where must probably SBA-15 hexagonal pores are present and dark areas where a high Cu/Ce ratio was detected by EDX. In the clear areas, the signals associated with the presence of Cu and Ce are less intense than those observed in the dark areas.

Table 1
Average crystallite size and strains calculated using Rietveld refinement data. Cerianite: CeO_2, lattice parameter: 5.412 Å, tenorite: CuO, zirconia: ZrO_2.

Sample	Phase	Lattice parameter (Å)	D_i (nm)	ε_i (%)	R_{wp}
SBAZr10Ce20Cu6	Cerianite	5.415(4)	14.1	0.16	5.56
	Tenorite		59.0	0.16	
SBACe20Cu6	Cerianite	5.414(4)	11.8	0.06	4.34
	Tenorite		32.5	0.08	
$SBAZrO_2$10Ce20Cu6	Cerianite	5.412(5)	20.9	0.02	4.49
	Tenorite		103.0	0.16	
	Zirconia		22.1	0.67	

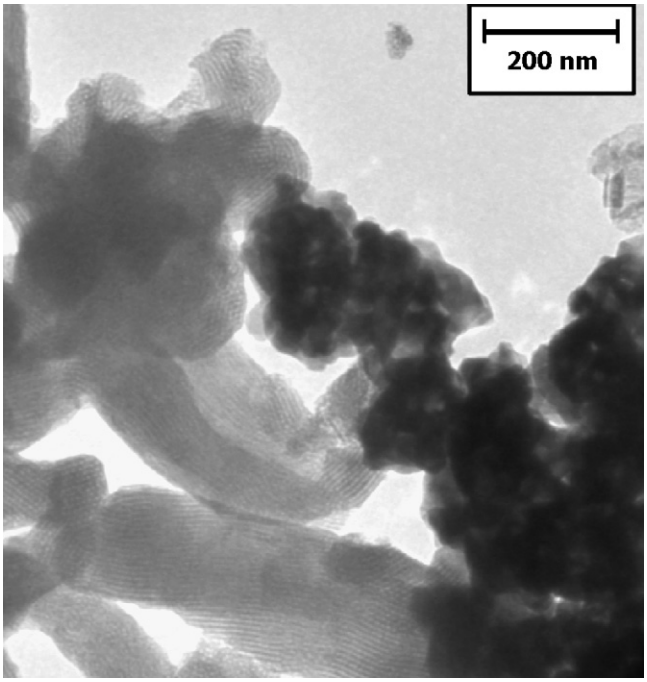

Fig. 5. TEM image of the sample SBAZr10Ce20Cu6.

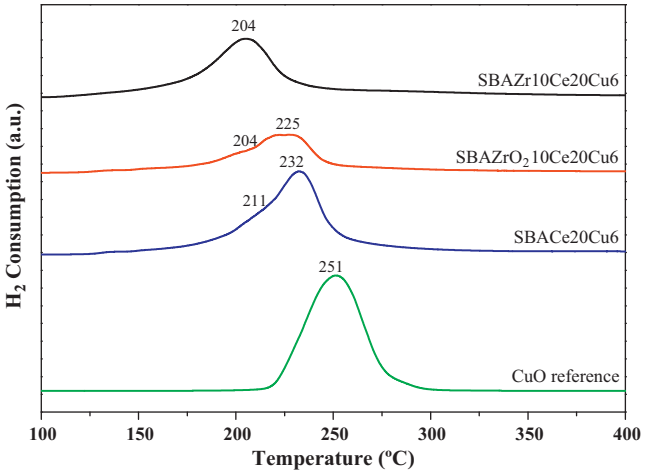

Fig. 6. Temperature programmed reduction (H_2-TPR) profiles of the fresh samples, compared with a CuO reference.

3.3.1. H_2-TPR and XPS – redox behaviour

The redox behavior of catalysts can be studied with H_2-TPR and XPS techniques. The CO-PROX reaction was studied by several authors [26–29] and a Mars-Van Kravelen type reaction mechanism is widely accepted and a correlation between redox and catalytic properties is strongly suggested. These properties are attributed to the interactions between CuO and CeO_2 interfacial sites, as previously discussed [20]. H_2-TPR studies showing the reducibility of metallic species were widely used in catalyst characterization, especially when metallic oxides are involved in the active phase. The profiles of the samples are shown in Fig. 6 and compared with a CuO reference using the equivalent amount of copper.

The reduction of CeO_2 and ZrO_2 [10–12] cannot occur in the studied temperature range. The reduction of CuO supported on CeO_2 and CeO_2–ZrO_2 was observed to start at a much lower temperature (>50 °C) than bulk CuO. All the consumption of hydrogen in these samples is associated to the reduction of copper species [8]. The TPR curve of the CuO reference shows a H_2 consumption peak centred at 251 °C. All the supported samples show the maxima of the H_2 consumption peaks at lower temperatures as a function of the dispersion of Zr over the support. The TPR curve of the sample without Zr (SBACe20Cu6) shows a maximum at 232 °C and a shoulder at 211 °C. The incorporation of high dispersed ZrO_2 on the surface of the support increases the dispersion of Cu and Ce species, giving rise to a shift of the maximum of the TPR curve at a lower temperature (225 °C) and a shoulder at 204 °C. Finally, when Zr is incorporated in the structure of the support (SBAZr10) the temperature of the maximum of the curve decreases to 204 °C.

XPS was used to study the chemical state of the elements and their relative abundance at catalyst surface. Ce 3*d* and Cu 2*p* signals were of special interest to know the chemical state of the active phase of the fresh and used catalysts.

Cu 2*p* core levels spectra for fresh and used catalysts are shown in Fig. 7. A broad Cu $2p_{3/2}$ signal composed of two contributions at 932.8 and 934.8 eV with a shake-up satellite in the 940–945 eV region were observed for all the catalysts. The high binding energy contribution (934.8 eV) could be ascribed to the presence of CuO particles [8]. The second contribution at 932.8 eV can be assigned to reduced copper or small clusters of copper interacting with the support or with ceria. These observations are confirmed by XRD (Fig. 3) and TPR-H_2 (Fig. 6) by the presence of the shoulder at low reduction temperature.

After reaction, all the catalysts show a similar behavior, the partial reduction of copper species are highly denoted and could be estimated by the ratio between the intensity of the shake-up satellite peak and the main Cu $2p_{3/2}$ peak, with a significant reduction of this ratio for used catalyst. All fresh catalysts show a I_{sat}/I_{mp} value lower than that observed for CuO (0.55), indicating the presence of partially reduced copper species [8,12] formed by the interaction with ceria species [19,20]. These ratios are summarized in Table 3, showing a lower reduction degree in the catalyst with the SBAZr10 support.

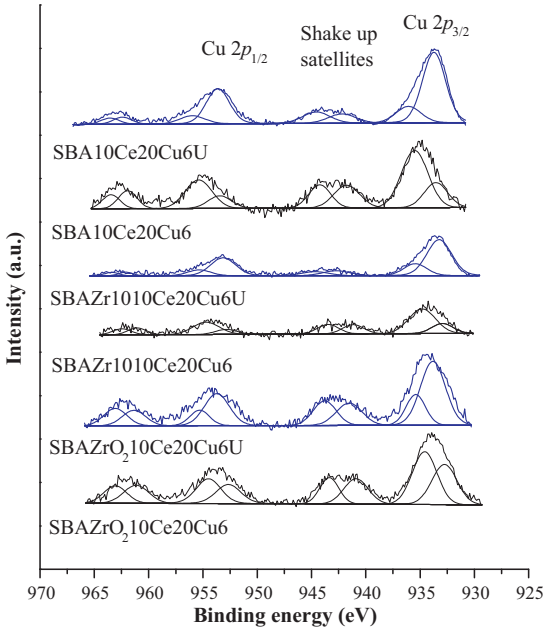

Fig. 7. Cu 2*p* photoelectron profiles of fresh and used (U) samples. CO-PROX operating conditions: 50% H_2, 1.25% CO, 1.25% O_2, He balanced, $\lambda = 2$, GHSV = 22 000 h^{-1}.

Fig. 8 shows the Ce 3*d* core level spectra for the fresh and used SBAZr10Ce20Cu6 catalyst as an illustrative example. The core level Ce 3*d* signal is composed by several contributions and was early studied by Burroughs et al. [30], and several authors [31–33] used the nomenclature initially proposed. The core level of Ce 3*d* signal of ceria is composed by six contributions ν_0, ν_1, and ν_2 (Ce $3d_{5/2}$) and ν'_0, ν'_1, and ν'_2 (Ce $3d_{3/2}$) that correspond to Ce^{4+} 3*d* final states and four peaks υ_0, and υ_1 (Ce $3d_{5/2}$) and υ'_0, and υ'_1 (Ce $3d_{3/2}$) corresponding to Ce^{3+} 3*d* final states. These final states are caused by the hybridization between the Ce 4*f* levels and O 2*p* states. Although the Ce 3*d* core level spectra are complex, an easy relation (Eq. (5)) can be used to estimate the amount of surface Ce^{3+}:

$$Ce^{3+}(\%) = \frac{S(Ce^{3+})}{S(Ce^{3+} + Ce^{4+})} = \frac{S(\upsilon_i) + S(\upsilon'_i)}{S(\upsilon_i) + S(\upsilon'_i) + S(\nu_i) + S(\nu'_i)} \times 100 \quad (5)$$

Fig. 8 shows the deconvolution of Ce 3*d* core level signal for the fresh and used SBAZr10Ce20Cu6 catalysts. The contribution of υ_0 and υ'_0 corresponding to Ce^{3+} $3d^9 4f^1 O2p^6$ final state at 880.5 and 989.8 eV are not considered due to low intensities of Ce 3*d* signal. Both Ce^{3+} and Ce^{4+} species are present before and after PROX reaction for all the catalysts. The Ce^{3+} percentages are summarized on Table 3,

Table 3
Redox parameters of fresh and used catalysts, calculated using data of Cu 2*p*, Zr 3*d* and Ce 3*d* regions.

Sample	Zr/Ce	Cu/Ce	%Ce^{3+}	Cu_{red}/Cu_{tot}	I_{sat}/I_{mp}
SBAZr10Ce20Cu6	0.6	1.0	21.5	0.23	0.45
SBAZr10Ce20Cu6U	0.3	0.9	22.0	0.68	0.25
SBACe20Cu6	0	0.7	17.5	0.26	0.45
SBACe20Cu6U	0	0.6	25.8	0.69	0.19
SBAZrO2 10Ce20Cu6	3.1	1.6	16.5	0.20	0.48
SBAZrO2 10Ce20Cu6U	3.2	1.9	15.6	0.73	0.27

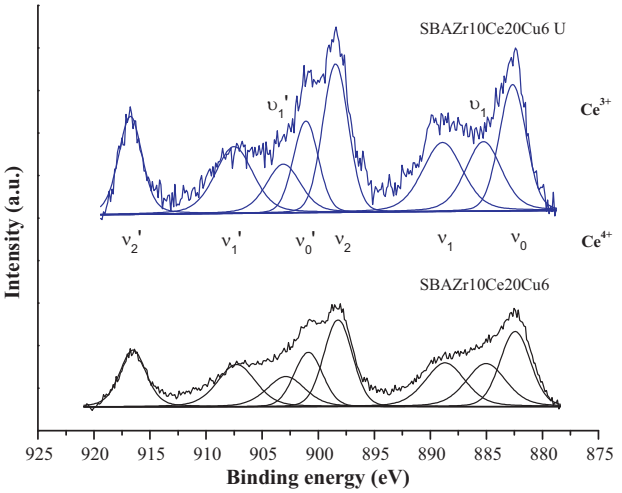

Fig. 8. High resolved Ce 3*d* photoelectron profiles of SBAZr10Ce20Cu6 fresh and used (U). Operation conditions: 50% H_2, 1.25% CO, 1.25% O_2, He balanced, $\lambda = 2$, GHSV = 22 000 h^{-1}.

showing a increase of Ce^{3+} after reaction due to partial reduction of the catalyst. If all the percentages are compared the catalyst with SBAZr10 support shows a lower reduction degree after reaction and the best catalytic performance.

The presence of surface carbonates was detected at 288.8 eV in the C 1*s* core level signal close to the reference signal of adventitious carbon at 284.8 eV. The presence of surface carbonates is always observed on the surface of lanthanide oxides. The O 1*s* core level spectra show an asymmetric peak that can be decomposed in two contributions at 529.8 and 532.7 eV assigned to the metallic oxides and to silica, respectively. Si 2*p* and Zr $3d_{5/2}$ core levels spectra have maxima at 103.0 eV and 182.3 eV, assigned to silica and Zr^{4+}, respectively. These XPS data in addition to the XRD data confirm that the catalysts are quite stable in catalytic operative conditions.

4. Conclusions

Zirconium doped SBA-15 appear to be good supports for the catalytic system CuO_x–CeO_2 to be used in the CO-PROX, due to the positive synergic effect of the dispersion of the active phases and their reducibility, as demonstrated by H_2-TPR and XPS studies. Most probably the organized surface of the support helps to provide a high dispersion of the nanometric size active phases, improving the contact between the particle interfaces, which were archived as active sites.

Acknowledgements

The Spanish authors appreciate the financial support by the project MAT09-10481 (Ministerio de Ciencia e Innovación, Spain), FEDER funds and by the project FQM 01661 (Proyecto de Excelencia de la Junta de Andalucía, Spain).

References

[1] F. Mariño, B. Schönbrod, M. Moreno, M. Jobbágy, G. Baronetti, M. Laborde, Catal. Today 133–135 (2008) 735.
[2] C. Song, Catal. Today 77 (2002) 17.
[3] R.M. Navarro, M.A. Peña, J.L.G. Fierro, Chem. Rev. 107 (2007) 3952.
[4] P. Zhu, J. Li, Q. Huang, S. Yan, M. Liu, R. Zhou, J. Nat. Gas Chem. 18 (2009) 346.
[5] T.V. Choudhary, D.W. Goodman, Catal. Today 62 (2002) 249.
[6] A. Kirubakaran, S. Jain, R.K. Nema, Renew. Sust. Energy Rev. 13 (2009) 2430.
[7] N. Bion, F. Epron, M. Moreno, F. Mariño, D. Duprez, Top. Catal. 51 (2008) 76.
[8] G. Avgouropoulos, T. Ioannides, Appl. Catal. B 67 (2006) 1.
[9] D. Gamarra, G. Munuera, A.B. Hungría, M. Fernández-García, J.C. Conesa, P.A. Midgley, X.Q. Wang, J.C. Hanson, J.A. Rodríguez, A. Martínez-Arias, J. Phys. Chem. C 111 (2007) 11026.
[10] E. Moretti, M. Lenarda, L. Storaro, A. Talon, R. Frattini, S. Polizzi, E. Rodríguez-Castellón, A. Jiménez-López, Appl. Catal. B 72 (2007) 149.
[11] E. Moretti, M. Lenarda, L. Storaro, A. Talon, T. Montanari, G. Busca, E. Rodríguez-Castellón, A. Jiménez-López, M. Turco, G. Bagnasco, R. Frattini, Appl. Catal. A 335 (2008) 46.
[12] E. Moretti, L. Storaro, A. Talon, R. Moreno-Tost, E. Rodríguez-Castellón, A. Jiménez-López, M. Lenarda, Catal. Lett. 129 (2009) 323.
[13] D. Gamarra, A. Hornés, Zs. Koppàny, Z. Schay, G. Munuera, J. Soria, A. Martínez-Arias, J. Power Sources 169 (2007) 110.
[14] A. Martínez-Arias, J. Soria, R. Cataluña, J.C. Conesa, V. Cortés Corberán, Stud. Surf. Sci. Catal. 116 (1998) 591.
[15] W. Liu, A.F. Sarofim, M. Flytzani-Stephanopoulos, Chem. Eng. Sci. 49 (1995) 4871.
[16] A. Martínez-Arias, M. Fernández-García, O. Gálvez, J.M. Coronado, J.A. Anderson, J.C. Conesa, J. Soria, G. Munuera, J. Catal. 195 (2000) 207.
[17] B. Skårman, D. Grandjean, R.E. Benfield, A. Hinz, A. Andersson, L.R. Wallenberg, J. Catal. 211 (2002) 119.
[18] A.N. Ilichev, A.A. Firsova, V.N. Korchak, Kinet. Catal. 47 (2006) 585.
[19] D. Gamarra, A. Martínez-Arias, J. Catal. 263 (2009) 189.
[20] A. Martínez-Arias, D. Gamarra, M. Fernández-García, A. Hornés, P. Bera, Zs. Koppány, Z. Schay, Catal. Today 143 (2009) 211.
[21] J.L. Ayastuy, A. Gurbani, M.P. González-Marcos, M.A. Gutiérrez-Ortiz, Int. J. Hydrogen Energy 35 (2010) 1232.
[22] K. Szczodrowski, B. Prélot, S. Lantenois, J. Zajac, M. Lindheimer, D. Jones, A. Julbe, A. van der Lee, Micropor. Mesopor. Mater. 110 (2008) 111.
[23] M. Gómez-Cazalilla, J.M. Mérida-Robles, A. Gurbani, E. Rodríguez-Castellón, A. Jiménez-López, J. Solid State Chem. 180 (2007) 1.
[24] H.M. Rietveld, J. Appl. Crystall. 2 (1969) 165.
[25] S. Poulston, P.M. Parlet, P. Stone, M. Bowker, Surf. Interf. Anal. 24 (1996) 811.
[26] Y. Liu, Q. Fu, M.F. Stephanopoulos, Catal. Today 93–95 (2004) 241.
[27] G. Sedmak, S. Hocevar, J. Levec, J. Catal. 213 (2003) 135.
[28] A. Martínez-Arias, A.B. Hungría, M. Fernández-García, J.C. Conesa, G. Munuera, J. Phys. Chem. B 108 (2004) 17983.
[29] H.C. Lee, D.H. Kim, Catal. Today 132 (2008) 109.
[30] P. Burroughs, A. Hamnet, A.F. Orchard, G. Thornton, J. Chem. Soc. Dalton 17 (1976) 1686.
[31] L. Qiu, F. Liu, L. Zhao, Y. Ma, J. Yao, Appl. Surf. Sci. 252 (2006) 4931.
[32] X. Tang, B. Zhang, Y. Li, Y. Xu, Q. Xin, W. Shen, Appl. Catal. A 288 (2005) 116.
[33] F. Zhang, P. Wang, J. Koberstein, S. Khalid, S. Chan, Surf. Sci. 563 (2004) 74.